Numerical Analysis of the Formability of an Aluminum 2024 Alloy Sheet and Its Laminates with Steel Sheets

HIROHIKO TAKUDA and NATSUO HATTA

A criterion for ductile fracture is applied to the formability prediction of an aluminum 2024 alloy sheet and its laminated composite sheets. Axisymmetric deep-drawing processes of the 2024 sheet and the laminates clad by mild steel sheets are simulated by the finite-element method. From the calculated distributions and histories of stress and strain, the fracture initiation site and the forming limit are predicted by means of the ductile fracture criterion. The predictions so obtained are compared with experimental observations. The results show that the fracture initiation in the 2024 sheet with no appearance of necking is successfully predicted by the present numerical approach. Furthermore, it is found that the formability of the 2024 sheet is improved by sandwiching it with the mild steel sheets.

I. INTRODUCTION

THE precipitate-hardening aluminum 2024 alloy has high strength, superior to that of normal steels, and is commonly used as a light structural material. However, the forming products of the 2024 sheet are still limited. The press forming of the 2024 sheet is difficult, although the ductility itself is not so bad. In forming processes of the 2024 sheet, fracture often occurs without any obvious necking phenomenon.[1] In order to find the forming method and conditions suitable for a certain sheet, the forming limit, *i.e.*, the fracture initiation in sheet-forming processes, has to be correctly predicted. Although many studies on fatigue cracking have been carried out for the 2024 sheet,[2–6] few studies have been found where the forming limit in practical forming processes of the 2024 sheet is numerically analyzed.

In sheet metal forming, the forming limit is generally determined by the onset of localized necking, because the sheet tears immediately after the onset. Therefore, the conventional analytical methods used to predict the forming limit are based on the tensile instability or bifurcation theories.[7–10] However, these analytical methods are not applicable to the 2024 sheet, which breaks suddenly without any necking phenomenon preceding the forming limit. Needless to say, it is even more difficult to predict by conventional approaches the forming limit of the laminates composed of the 2024 sheet.

In the present study, therefore, another approach is applied to the prediction of the forming limit of the 2024 sheet. The fracture initiation in sheet-forming processes is predicted by the finite-element simulation combined with a criterion for ductile fracture. The calculations are carried out for axisymmetric deep drawing of the 2024 sheet and for its laminates clad by mild steel sheets. The validity of the predictions is examined by comparing them to the experimental results. Furthermore, the possibility of improving the formability of the 2024 sheet by laminating it with steel sheets is examined.

HIROHIKO TAKUDA, Associate Professor, and NATSUO HATTA, Professor, are with the Department of Energy Science and Technology, Kyoto University, Kyoto 606-8501, Japan.

Manuscript submitted December 23, 1997.

II. MATERIALS AND LAMINATED COMPOSITE SHEETS

The chemical composition of the aluminum 2024-T4 alloy sheet used in this study is indicated in Table I. The sheet thickness is 1.0 mm.

Uniaxial tension tests were carried out at 0, 45, and 90 deg to the rolling direction. The gage length and width were 50 and 12.5 mm, respectively. The relations between the tensile force and the elongation are shown in Figure 1. The decrease in the tensile force before fracture is not observed in Figure 1, and it shows fracture initiation in the tensile specimen with no obvious necking phenomenon. The tensile properties are indicated in Table II, with average values in the three directions. The true stress-strain (σ-ε) relation of the 2024 sheet can be approximated by the work-hardening exponent (n) as

$$\sigma = K\varepsilon^n \qquad [1]$$

where K is a constant. Although the 2024 sheet has the considerably high work-hardening exponent of 0.19, the elongation is only 17 pct (0.16 in true strain) and is even smaller than the n value.

The laminated composite sheets were made as follows. The 2024 sheet was clad on one or both sides by a mild steel sheet (SPCC) with a thickness of 0.3 mm (Figure 2). The chemical composition and the tensile properties of the steel sheet are indicated in Tables I and II, respectively. The cladding was carried out by adhesive bonding through a rolling mill using a polyurethane resin. It was ascertained by microscopic sectional observation of the laminates that there was no thickness change, *i.e.*, no plastic deformation occurred in the 2024 and the steel sheets through bonding, and that the thickness of the resin layer ranged between only 10 and 30 μm.

Table III shows the tensile strength and the elongation of the two-ply and three-ply laminated composite sheets in uniaxial tension tests.

Table I. Chemical Compositions of Materials (Mass Percent)

	Si	Fe	Cu	Mn	Mg	Cr	Zn	Ti	Al
A2024	0.07	0.20	4.70	0.58	1.40	0.02	0.04	0.03	bal
	C	Si	Mn	P	S	Al	N	Fe	
SPCC	0.051	0.016	0.220	0.016	0.015	0.025	0.002	bal	

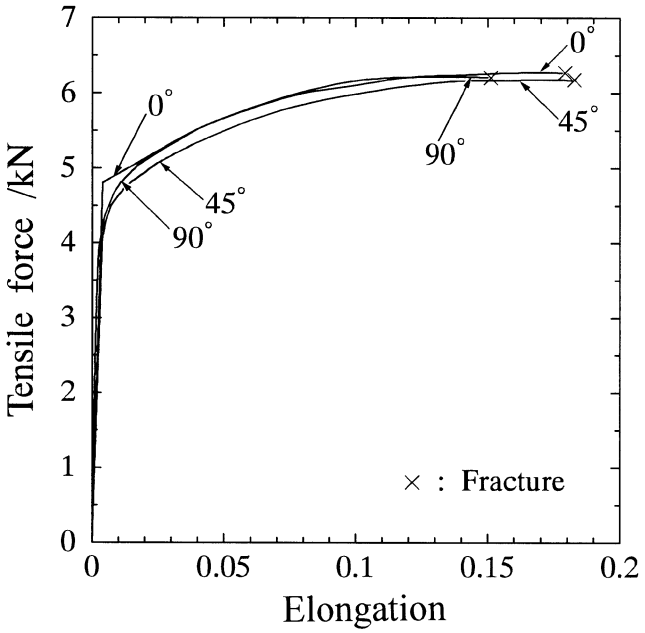

Fig. 1—Relation between tensile force and elongation in uniaxial tension tests of the aluminum alloy 2024 sheet.

Table II. Tensile Properties of Materials

	A2024	SPCC
Tensile strength, MPa	479	355
Elongation, pct	17	39
K value, MPa	749	615
Work-hardening exponent, *n*	0.19	0.20
Normal anisotropy parameter, *r*	0.78	1.41

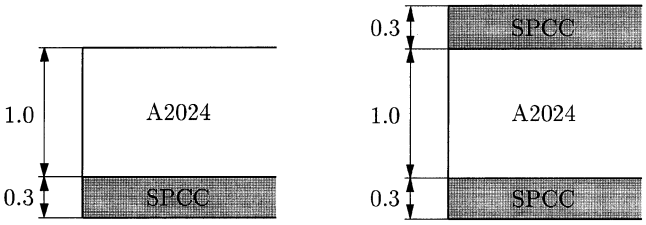

Fig. 2—Two-ply and three-ply laminates composed of the 2024 and SPCC sheets.

III. DUCTILE FRACTURE CRITERION

Some criteria for ductile fracture have been proposed empirically as well as theoretically.[11] In the field of bulk forming, the criteria for ductile fracture have been commonly used to predict the forming limit.[12–15] In the criteria, the occurrence of ductile fracture is estimated by the macroscopic stress and strain during forming. Oyane *et al.*[16] have proposed the criterion allowing for history of hydrostatic stress affecting the occurrence of the ductile fracture as

$$\int_0^{\bar{\varepsilon}_f} \left(\frac{\sigma_m}{\bar{\sigma}} + C_1\right) d\bar{\varepsilon} = C_2 \qquad [2]$$

where $\bar{\varepsilon}_f$ is the equivalent strain at which the fracture occurs, σ_m is the hydrostatic stress, $\bar{\sigma}$ is the equivalent stress, $\bar{\varepsilon}$ is the equivalent strain, and C_1 and C_2 are the material constants.

In this study, we apply the aforementioned criterion by Oyane *et al.* to the prediction of the formability of the 2024 sheet and its laminates clad by steel sheets. To determine the material constants C_1 and C_2 in Eq. [2], the destructive tests have to be operated under at least two types of stress conditions. Accordingly, in addition to the uniaxial tension tests, plane strain tension tests were carried out. Table IV shows the fracture strains in the tensile direction (ε_{1f}) derived from the measured reductions of area in uniaxial and plane strain tension tests. The material constants C_1 and C_2 are evaluated as follows.

Hill's yield criterion for anisotropic materials[17] is expressed as

$$F(\sigma_y - \sigma_z)^2 + G(\sigma_z - \sigma_x)^2 + H(\sigma_x - \sigma_y)^2 + 2L\tau_{yz}^2 + 2M\tau_{zx}^2 + 2N\tau_{xy}^2 = \frac{2}{3}(F + G + H)\bar{\sigma}^2 \qquad [3]$$

where F, G, H, L, M, and N are the anisotropy parameters. When no planar anisotropy of the sheet is assumed in Eq. [3], the terms in Eq. [2] are expressed at uniaxial and plane strain tension states as

$$\frac{\sigma_m}{\bar{\sigma}} = \frac{1}{3}\sqrt{\frac{2(2 + r)}{3(1 + r)}}, \quad d\bar{\varepsilon} = \sqrt{\frac{2(2 + r)}{3(1 + r)}}\, d\varepsilon_1 \quad \text{(uniaxial)} \qquad [4]$$

$$\frac{\sigma_m}{\bar{\sigma}} = \frac{1}{3}\sqrt{\frac{2(2 + r)(1 + 2r)}{3(1 + r)}}, \quad d\bar{\varepsilon} = \sqrt{\frac{2(2 + r)(1 + r)}{3(1 + 2r)}}\, d\varepsilon_1 \quad \text{(plane strain)} \qquad [5]$$

where r is the normal anisotropy parameter, and ε_1 is the strain in the tensile direction in tension tests.

Provided that the relations of Eqs. [4] and [5] are maintained until fracture initiation, the material constants C_1 and C_2 are approximately obtained from Eqs. [2], [4], and [5] and ε_{1f} in Table IV, as indicated in Table V.

Table III. Tensile Properties of Two-Ply and Three-Ply Laminates

	Two-Ply	Three-Ply
Tensile strength, MPa	444	425
Elongation, pct	21	22

Table IV. Fracture Strains in Tensile Direction, ε_{1f}, of Materials in Uniaxial and Plane Strain Tension Tests

	A2024	SPCC
ε_{1f} (uniaxial)	0.19	0.77
ε_{1f} (plane strain)	0.14	0.35

Table V. Material Constants C_1 and C_2 in Equation [2]

	A2024	SPCC
C_1	0.61	0.057
C_2	0.18	0.29

IV. EXPERIMENTAL AND SIMULATION METHODS OF DEEP DRAWING

For the aforementioned 2024 and laminated composite sheets, the cylindrical deep-drawing tests are carried out using a flat-headed punch, and they are simulated by the rigid-plastic finite-element method.[18] Figure 3 shows schematically the tools for the deep-drawing tests. The diameter and the profile radius of the punch are 40 and 4 mm, respectively. The diameters of the dies used are 42.5, 43, and 44 mm for the 2024 single-layer sheet, the two-ply laminate, and the three-ply laminate, respectively. The profile radius of the dies is 8 mm. Circular blanks, with various diameters (d_0) in 1-mm intervals, are prepared. Both faces of the blanks are well lubricated with sprayed wax. The blank holder force for each blank is given according to Siebel's equation.[19]

In the simulation, the axisymmetric deformation with no planar anisotropy is assumed, while the normal anisotropy of the sheet is taken into consideration. The finite-element method is formulated on the basis of the plasticity theory for a slightly compressible material, by modifying Hill's yield criterion as

$$\bar{\sigma} = \sqrt{\frac{3}{2(2+r)}\{r(\sigma_R-\sigma_\theta)^2+(\sigma_\theta-\sigma_Z)^2+(\sigma_Z-\sigma_R)^2\} + 3\tau_{RZ}^2 + g\left\{\frac{1}{1+2r}(r\sigma_R+r\sigma_\theta+\sigma_Z)\right\}^2} \quad [6]$$

where g is a small positive constant (equal to 0.01) for slight compressibility. By the slight compressibility, the stress components can be calculated directly from the strain-rate components, and, also, the condition of incompressibility is approximately satisfied. The literature[18] should be referred to for details of the basic equations of the finite-element method. Meshing is also carried out in the thickness direction using the quadrilateral solid elements (Figure 3), so that the material change in the thickness direction of the laminate can be taken into consideration. The existence of the resin layer is neglected, and no slip between the composing sheets is assumed. The coefficient of friction between the tool and the sheet is assumed to be 0.05.

Then, the criterion for ductile fracture is applied as follows.

Rewriting Oyane's ductile fracture criterion (Eq. [2]), we get the integral

$$I = \frac{1}{C_2}\int_0^{\bar{\varepsilon}}\left(\frac{\sigma_m}{\bar{\sigma}}+C_1\right)d\bar{\varepsilon} \quad [7]$$

Using the values of σ_m, $\bar{\sigma}$, and $d\bar{\varepsilon}$ obtained by the finite-element simulation and the material constants C_1 and C_2 in Table V, the integral I is calculated for each element and each deformation step. The condition of fracture is satisfied when and where the integral I amounts to 1. One deformation step is set to correspond to the punch stroke of about 0.1 mm in the present simulation.

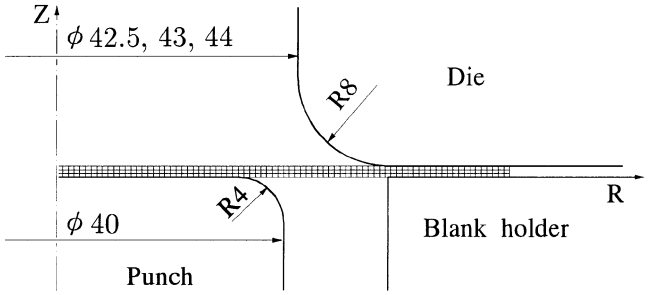

Fig. 3—Dimensions of tools for deep drawing tests.

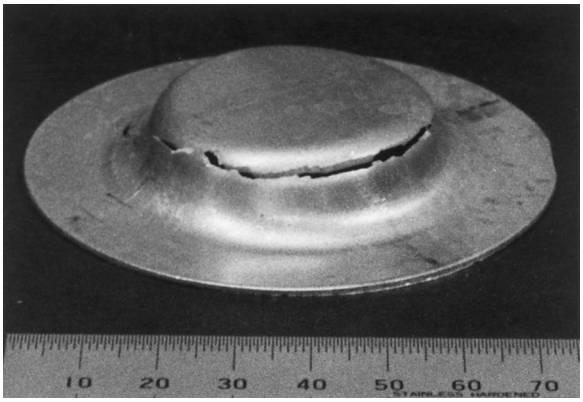

Fig. 4—Fracture around punch corner in deep drawing test of the 2024 sheet with d_0 of 80 mm.

V. RESULTS

Figure 4 shows the experimentally observed fracture in a deep-drawing test for the 2024 single layer sheet with an initial blank diameter (d_0) of 80 mm. When the blank diameter is much larger than the maximum drawable one, the fracture occurs around the punch corner, as is shown in Figure 4. Similar to the fracture in the aforementioned uniaxial tension test, the fracture in deep drawing, also occurs with no obvious localized necking or thinning phenomenon.

Figure 5 shows the result of the finite-element simulation combined with the ductile fracture criterion for the aforementioned case. The left part (a) of Figure 5 illustrates the transition of the blank profile with the increase in the punch stroke (s). The localized necking does not appear in the blank profile, and it seems as if the blank could be drawn without fracture. However, the fracture actually occurs as in Figure 4. The right part (b) of Figure 5 shows the evolution of the distribution of the integral I of the fracture criterion. The horizontal and the vertical axes of Figure (b) indicate the initial radial position from the blank center and the average value of I at the corresponding radial position, respectively. Figure 5(b) shows that the integral I around the punch corner amounts to 1 at the punch stroke of 12.4 mm and predicts the fracture initiation of Figure 4. Note that the numerical result after the fracture initiation shown in Figure 5 is, accordingly, not valid.

The remarkable feature of the 2024 sheet in deep drawing is the fracture phenomenon shown in Figure 6. When

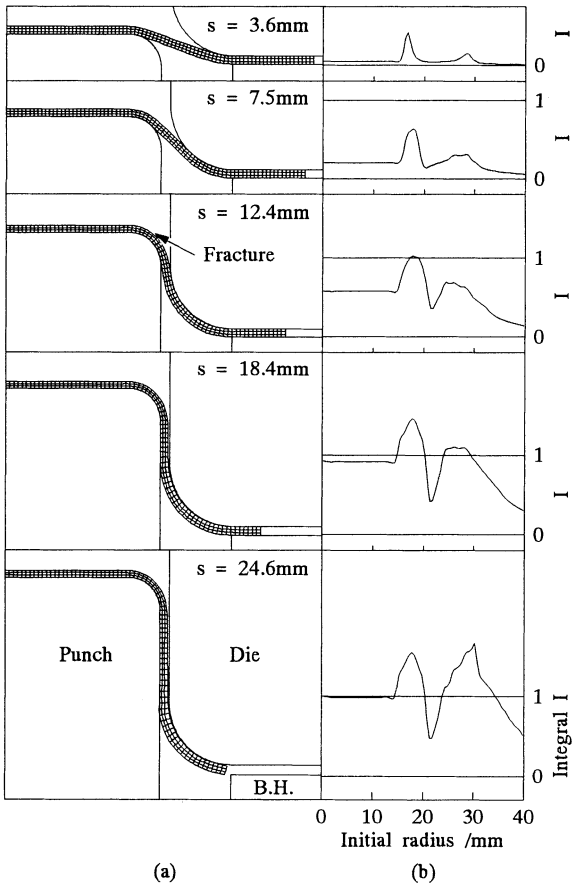

Fig. 5—Calculated result of deep drawing for the 2024 sheet and d_0 = 80 mm.

Fig. 6—Fracture at sidewall in deep drawing test for the 2024 sheet and d_0 = 70 mm.

the blank diameter is slightly larger than the maximum drawable one, the fracture occurs at the sidewall of the drawn cup, while no fracture occurs around the punch corner. Figure 6 shows the experimentally observed fracture initiation at the sidewall at a later stage of deep drawing, for d_0 = 70 mm. Figure 7 shows, in the same way as Figure 5, the calculated transitions of the blank profile and the distribution of the integral I. Although the integral I around the punch corner increases at the early stage of deep drawing, it does not amount to 1. On the other hand, the integral I at the sidewall increases mainly at the later stage, until

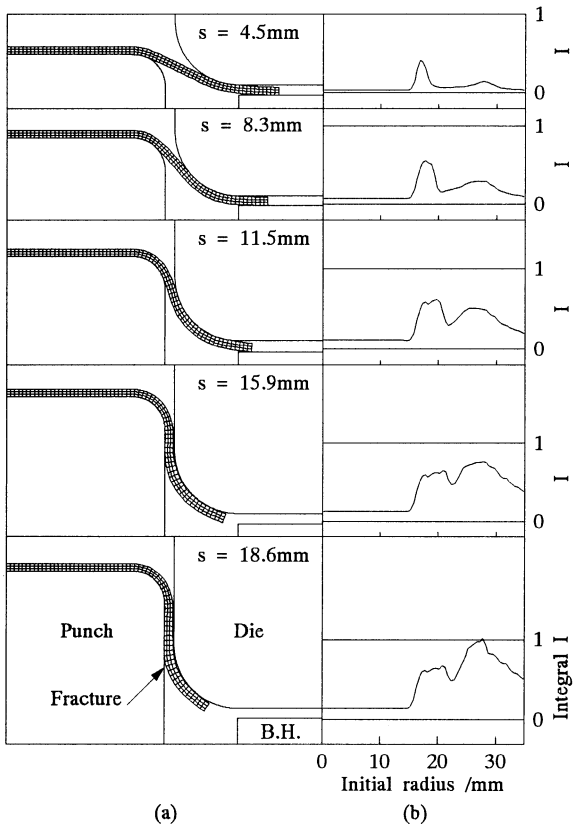

Fig. 7—(*a*) and (*b*) Calculated result for the 2024 sheet and d_0 = 70 mm.

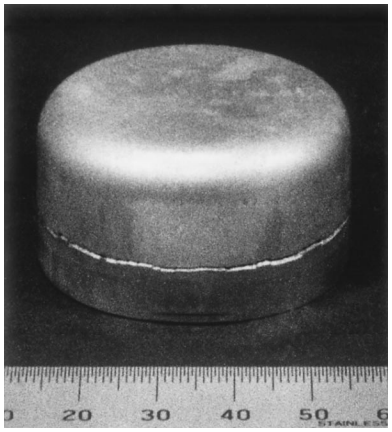

Fig. 8—Fracture at sidewall in deep drawing test of the two-ply laminate in case where the SPCC layer is set on the punch side (d_0 = 70 mm).

the fracture occurs there. The good correspondence between the experimental and calculated results of Figures 6 and 7 exhibits the effectiveness and the validity of the present numerical approach.

The limiting drawable diameter of the laminates composed of the 2024 and SPCC sheets also depends upon the fracture at the sidewall in the 2024 layer. Figure 8 shows a specimen after a deep-drawing test using a two-ply laminate with d_0 = 70 mm. Although the cup is formed with the support of the SPCC layer set on the punch side, the fracture is observed at the sidewall in the 2024 layer.

The calculated results of the deep drawing of the laminated composite sheets are illustrated in Figures 9 through

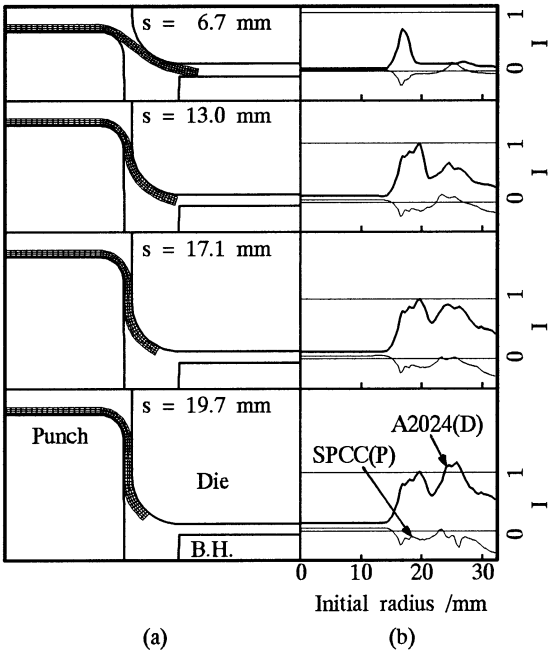

Fig. 9—(*a*) and (*b*) Calculated result for the two-ply laminate in case where the SPCC layer is set on the punch side (d_0 = 70 mm).

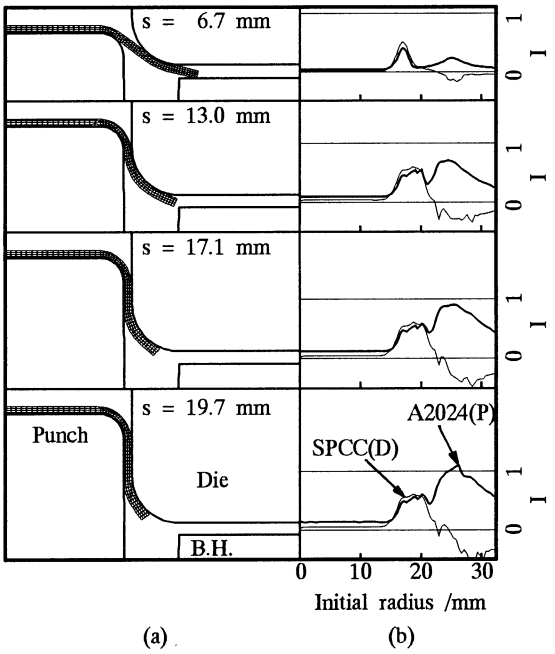

Fig. 10—(*a*) and (*b*) Calculated result for the two-ply laminate in case where the SPCC layer is set on the die side (d_0 = 70 mm).

11. The right part (b) of each figure shows the distributions of the *I* integrals of the layers composing the laminates. The labels ''P'' and ''D'' in the figures indicate the layers on the punch and the die sides, respectively. There are two types of deep-drawing tests for the two-ply laminates, depending upon whether the SPCC layer is set on the punch or the die side. The experimental result shown in Figure 8 corresponds to the case of Figure 9. The distributions of the *I* integrals predict the fracture initiation only in the 2024 layer at the sidewall. The integral *I* around the punch corner barely remains below 1. Figure 10 also predicts the fracture

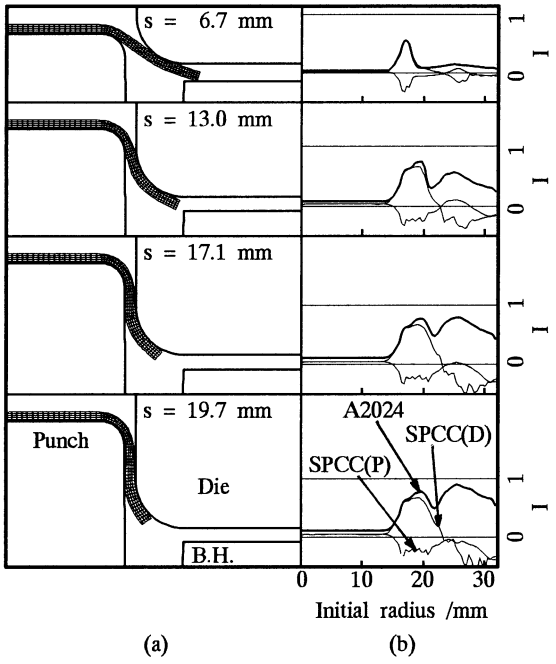

Fig. 11—(*a*) and (*b*) Calculated result for the three-ply laminate and d_0 = 70 mm.

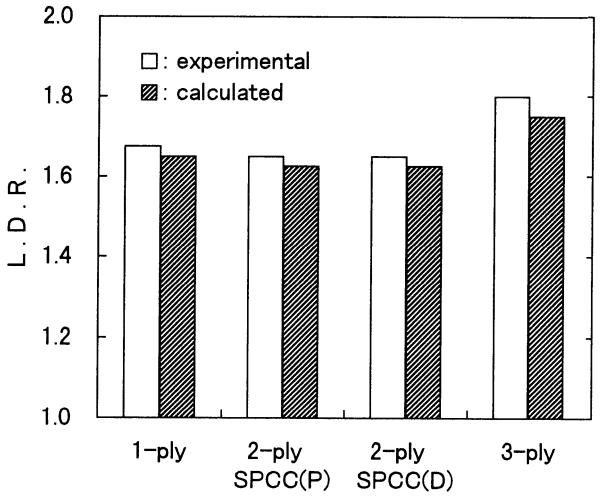

Fig. 12—Comparison between calculated and experimental limiting drawing ratios.

initiation for the reversed case of the two-ply laminate, while Figure 11 shows no fracture initiation for the three-ply laminate.

The limiting drawing ratios, predicted by assuming that the fracture occurs when and where the integral *I* of Eq. [7] amounts to 1, are compared to the experimental ones in Figure 12. The limiting drawing ratio (LDR) is defined as d_{0max}/d_p, where d_{0max} is the maximum initial diameter of the blank which is drawable without fracture and d_p is the punch diameter. Fairly good agreements are seen between the calculated and the experimental ratios, not only for the single-layer sheet, but also for the laminated composite sheets. It is found numerically, as well as experimentally, that the LDR of the three-ply laminate is somewhat larger than that of the single-layer sheet, while no improvement

in drawability is recognized for the cases of the two-ply laminate.

VI. CONCLUSIONS

To predict the forming limit of the aluminum 2024 alloy sheet, which breaks with no appearance of localized necking, the ductile fracture criterion was introduced into the finite-element simulation. Using the local stress and strain histories calculated by the rigid-plastic finite-element simulation, the fracture initiation was predicted by means of the fracture criterion. The calculations were carried out for axisymmetric deep drawing of the 2024 sheet and its laminates clad by mild steel sheets. The comparison to the experimental results showed that the fracture initiation sites and the forming limits were successfully predicted by the present approach. It was found that the drawability of the 2024 sheet could be improved by laminating with steel sheets on both sides.

ACKNOWLEDGMENTS

This study was financially supported by a Grand-in-Aid for Scientific Research (No. 09650784) from the Ministry of Education, Science and Culture of Japan. The authors thank the staff at the steel research laboratories of Nippon Steel Corporation for providing the laminated composite sheets.

REFERENCES

1. N. Kawai, T. Mori, M. Inoue, and Y. Liu: *Trans. Jpn. Soc. Mech. Eng.*, 1986, vol. 52C, pp. 1689-95.
2. S.D. Antolovich, A. Saxena, and G.R. Chanani: *Eng. Fract. Mech.*, 1975, vol. 7, pp. 649-52.
3. W.J. Mills and R.W. Hertzberg: *Eng. Fract. Mech.*, 1975, vol. 7, pp. 705-11.
4. T. Takamatsu and M. Ichikawa: *JSME Int. J.*, 1987, vol. 30, pp. 1035-41.
5. J. Zuidema and M. Mannesse: *Eng. Fract. Mech.*, 1991, vol. 40, pp. 105-17.
6. O. Partl and J. Schijve: *Int. J. Fatigue*, 1993, vol. 15, pp. 293-99.
7. H.W. Swift: *J. Mech. Phys. Solids*, 1952, vol. 1, pp. 1-18.
8. R. Hill: *J. Mech. Phys. Solids*, 1952, vol. 1, pp. 19-30.
9. Z. Marciniak and K. Kuczynski: *Int. J. Mech. Sci.*, 1967, vol. 9, pp. 609-20.
10. S. Stören and J.R. Rice: *J. Mech. Phys. Solids*, 1975, vol. 23, pp. 421-41.
11. S.E. Clift, P. Hartley, C.E.N. Sturgess, and G.W. Rowe: *Int. J. Mech. Sci.*, 1990, vol. 32, pp. 1-17.
12. K. Osakada and K. Mori: *Ann. CIRP*, 1978, vol. 27, pp. 135-39.
13. S.I. Oh, C.C. Chen, and S. Kobayashi: *Trans. ASME, J. Eng. Ind.*, 1979, vol. 101, pp. 36-44.
14. M. Ayada, T. Higashino, and K. Mori: *Advanced Technology of Plasticity*, K. Lange, ed., Springer-Verlag, Berlin, 1987, vol. 1, pp. 553-58.
15. M. Toda, T. Miki, S. Yanagimoto, and K. Osakada: *J. Jpn. Soc. Technol. Plasticity*, 1988, vol. 29, pp. 971-76.
16. M. Oyane, T. Sato, K. Okimoto, and S. Shima: *J. Mech. Working Technol.*, 1980, vol. 4, pp. 65-81.
17. R. Hill: *The Mathematical Theory of Plasticity*, Oxford University Press, Oxford, United Kingdom, 1950, pp. 318-21.
18. K. Osakada, J. Nakano, and K. Mori: *Int. J. Mech. Sci.*, 1982, vol. 24, pp. 459-68.
19. E. Siebel: *Stahl Eisen*, 1954, vol. 74, pp. 155-58.